

Article

# Composition versus Wear Behaviour of Air Plasma Sprayed NiCr–TiB<sub>2</sub>–ZrB<sub>2</sub> Composite Coating

Ning Zhang <sup>1</sup>, Nannan Zhang <sup>1,\*</sup> , Sheng Guan <sup>2</sup>, Shumei Li <sup>2</sup>, Guangwei Zhang <sup>2</sup> and Yue Zhang <sup>1</sup> 

<sup>1</sup> Department of Material Science and Engineering, Shenyang University of Technology, Shenyang 110870, China; zhangning201610034@sut.edu.cn (N.Z.); yuezhang@sut.edu.cn (Y.Z.)

<sup>2</sup> Dalian Huarui Heavy Industrial Special Spare Parts Co., Ltd., Dalian 116052, China; Guansheng@dhidcw.com (S.G.); LiSM@dhidcw.com (S.L.); lichao@dhidcw.com (G.Z.)

\* Correspondence: zhangnn@sut.edu.cn; Tel.: +86-242-549-6812

Received: 13 June 2018; Accepted: 5 August 2018; Published: 6 August 2018



**Abstract:** The NiCr–TiB<sub>2</sub>–ZrB<sub>2</sub> composite coating was deposited on the surface of blades made of steel (SUS304) using high-energy ball milling technology and air plasma spraying technology, which aimed to relieve the wear of the blades during operation. The influence of titanium diboride (TiB<sub>2</sub>) and zirconium diboride (ZrB<sub>2</sub>) on the microstructure and wear resistance of the coatings was investigated by X-ray diffraction, scanning electron microscopy, Vickers microhardness tester, and a wear tester. The results showed that the TiB<sub>2</sub> and ZrB<sub>2</sub> particles were unevenly distributed in the coatings and significantly increased the hardness and anti-wear, which contributed to their ultra-high hardness and extremely strong ability to resist deformation. The performance of the coatings was improved with the increase of the number of ceramic phases, while the hardness and wear resistance of the coating could reach their highest value when the TiB<sub>2</sub> and ZrB<sub>2</sub> respectively took up 15 wt.% of the total mass of the powder.

**Keywords:** TiB<sub>2</sub>; ZrB<sub>2</sub>; coating blade; anti-wear

## 1. Introduction

The coating of a blade has a crucial influence on the quality of fine art coated paper and coated white paper. However, with the further development of coating technology resulting in a higher production efficiency, the speed of the coating blade has also been increased from 5 to 16 m/s. The traditional carbon steel blade is gradually being replaced by a wear-resistant ceramic coating blade because its service life is too short, it is about 3–4 h, as a result of severe three-body abrasive wear. The process of changing blades and the running-in stage has reduced the efficiency of the coating production [1].

At present, countries around the world are using the oxide (Al<sub>2</sub>O<sub>3</sub>·TiO<sub>2</sub> and ZrO<sub>2</sub>) and carbide (Cr<sub>3</sub>C<sub>2</sub> and WC) ceramic blades produced by the three companies of BTG (Eclépens, Switzerland), GREEN COAT (Siheung, Korea), and PSK (Portland, OR, USA) [2]. The performance of oxide ceramic blades has been significantly improved compared to the carbon steel blades, as the main component of the coating is kaolin, which contains Al<sub>2</sub>O<sub>3</sub>·2SiO<sub>2</sub>·2H<sub>2</sub>O, CaCO<sub>3</sub>, TiO<sub>2</sub>, and so on. Furthermore, the intersolubility of the same materials is large. However, adhesion wear can easily occur between these oxide ceramics [3], and thus, the oxide ceramic coating is not very suitable for practical production applications. Tungsten carbide (WC) has a relatively high thermal conductivity [4] and the thermal conductivity rose linearly from 29.3 to 86 W/(m·K) when the temperature increased from 20 to 500 °C [5]. Therefore, it is easy to transfer a large amount of heat to the blade steel strip during the initial stage of contact between the blade and the paper, causing the blade edge to become uneven,

which is unfavorable for the production of coatings. The hardness of chromium carbide ( $\text{Cr}_3\text{C}_2$ ) is relatively low, and its wear resistance is far inferior to the WC [6–8]. Therefore, a new type of ceramic coating is urgently needed to solve these problems.

Boride ceramics ( $\text{TiB}_2$  and  $\text{ZrB}_2$ ) have a higher hardness (Moh's hardness of 9–10) and an outstanding wear resistance. Compared to WC ( $15.63 \text{ g/cm}^3$ ), boride ceramics have a density that is lower by about 75% ( $4.51$  and  $5.8 \text{ g/cm}^3$ ), and a lower thermal conductivity ( $24.3$ – $23.03 \text{ W/(m}\cdot\text{K)}$ ) and  $24.28$ – $41.87 \text{ W/(m}\cdot\text{K)}$  in the temperature range of  $20$ – $500 \text{ }^\circ\text{C}$  [9–11]. Therefore, boride ceramics are potential materials for replacing the oxides and carbide ceramics.

Jones et al. [12] prepared Fe(Cr)– $\text{TiB}_2$  coatings using self-propagation high-temperature synthesis (SHS) and high velocity oxygen-fuel spraying (HVOF) technology. They found that the wear-coefficient of a 30% FeCr– $\text{TiB}_2$  coating ( $7.235 \text{ }\mu\text{g/(m}\cdot\text{N)}$ ) was lower than that of a 17% Co–WC ( $10.707 \text{ }\mu\text{g/(m}\cdot\text{N)}$ ), 30% Fe(Cr)–TiC ( $9.061 \text{ }\mu\text{g/(m}\cdot\text{N)}$ ), and 25%  $\text{Cr}_3\text{C}_2$ –NiCr ( $19.069 \text{ }\mu\text{g/(m}\cdot\text{N)}$ ) coating. In addition, the wear rate of the  $\text{TiB}_2$ -based composite coating was only 50% of the TiC-based coating, and was far superior to other materials when the grinding material was abrasive silica. Xu et al. [13] used SHS and atmospheric plasma spraying technology to prepare ZrC– $\text{ZrB}_2$ /Ni composite coatings with a variety of different proportions of Ni. The study showed that the highest hardness of coating reached  $525 \pm 96 \text{ HV}_{0.1}$  and had the maximum resistance to wear when the content of Ni was 10%.

The thermal conductivity of  $\text{ZrB}_2$  is lower than that of the  $\text{TiB}_2$  coating, while the resistance to wear of  $\text{TiB}_2$  is better than that of the  $\text{ZrB}_2$  coating [14]. Most importantly, the addition of  $\text{TiB}_2$  and  $\text{ZrB}_2$  in the same coating can significantly improve its wear resistance [15–17]. Hence, the  $\text{TiB}_2$ – $\text{ZrB}_2$  ceramic composite coatings were the best choice to improve the quality of the coating blade. However, the pure ceramic is too brittle, so it is necessary to add a ductile metal (NiCr) with a good wettability to form a cermet composite material in order to better meet the use conditions [18,19]. Furthermore, plasma spraying is especially suitable for ceramic materials with a high melting point because of the higher flame temperature and faster jet speed of the plasma spraying. In this paper, the air plasma spraying technology was used to prepare a NiCr– $\text{TiB}_2$ – $\text{ZrB}_2$  composite coating, and its tribological properties were analyzed.

## 2. Materials and Methods

### 2.1. Feedstock Materials

Commercially available nickel chromium (NiCr),  $\text{TiB}_2$ ,  $\text{ZrB}_2$  powders, and SUS304 stainless steel were purchased in this study. The NiCr powder (Ti Metal Materials Co., Ltd., Changsha, China) was atomized into a spherical shape by an inert gas with an average size of  $50 \text{ }\mu\text{m}$ . The  $\text{TiB}_2$  and  $\text{ZrB}_2$  powders were obtained from Xiangtian Nano Materials Co., Ltd. (Shanghai, China) as irregular powders with an average particle size of  $50 \text{ }\mu\text{m}$ . The substrates (SUS304) were provided by Shenzhen Bao Metal Products Co., Ltd. (Shenzhen, China), which have dimensions of approximately  $30 \text{ mm} \times 50 \text{ mm} \times 5 \text{ mm}$ . The information on all of the feedstock materials is listed in Table 1.

**Table 1.** Composition of the raw materials (at.%).

Materials	Purity	Zr	Ti	B	Cr	Ni	Fe	C	Others
NiCr	99.0	–	–	–	19.86	80.08	–	0.01	Bal.
$\text{TiB}_2$	99.5	–	68.23	30.75	–	–	0.14	0.13	Bal.
$\text{ZrB}_2$	99.9	79.27	–	19.30	–	–	0.09	0.15	Bal.
SUS304	–	–	–	–	18.65	9.73	68.54	0.07	Bal.

### 2.2. Powder Preparation

The first stage of the experiment involved the preparation of NiCr– $\text{TiB}_2$ – $\text{ZrB}_2$  powders by the high-energy ball milling method. Firstly, we mixed the three types of powders in equal proportions, before the mixture of the powders and the same quality of agate balls (ball-to-powder weight ratio

of 1:1) were placed in the same agate jar with a high purity argon (99.999%) protection. This was then placed in the ball mill (XQM-0.4, Delixi Hangzhou Inverter Co., Ltd., Hangzhou, China) at 6.67 r/s for 640 min. The mixture was rested for 20 min every 80 min to maintain the powders at a lower temperature. After this, the moisture was removed from the powders in a digital electric blast dry oven (101A-2, Shanghai JinPing Instrument Co., Ltd., Shanghai, China). Finally, three different types of target cermet composite powders (NiCr (5 wt.%)–TiB<sub>2</sub> (5 wt.%)–ZrB<sub>2</sub>, NiCr (10 wt.%)–TiB<sub>2</sub> (10 wt.%)–ZrB<sub>2</sub>, and NiCr (15 wt.%)–TiB<sub>2</sub> (15 wt.%)–ZrB<sub>2</sub>) were prepared by adjusting the proportions of NiCr, TiB<sub>2</sub>, and ZrB<sub>2</sub>.

### 2.3. APS Spraying Experiments

The NiCr–TiB<sub>2</sub>–ZrB<sub>2</sub> composite coatings were prepared on the surface of the SUS304 using the SG-100DC plasma torch (Praxair 3710, Cleveland, OH, USA) and ball milled powders. The parameters of the spraying are summarized in Table 2. Prior to the spraying, one side of the substrate was grit-blasted with 0.6 mm of Al<sub>2</sub>O<sub>3</sub> particles to achieve the required experimental surface. The Ar served both as a protective gas and as a powder-feeding gas to reduce the degree of oxidation, while H<sub>2</sub> was used as a fuel gas to provide energy for the experiment during the process of spraying. The specimens were cut into small pieces to facilitate the investigation of the morphology and phase composition after the experiments.

**Table 2.** Operation parameters of plasma spraying.

Parameters	Value
Current (A)	600
Voltage (V)	40
Ar (dm <sup>3</sup> /s)	0.67
H <sub>2</sub> (dm <sup>3</sup> /s)	0.17
Powder feed rate (g/s)	0.58–0.75
Gun traverse speed (mm/s)	90
Spray distance (mm)	100
Pre-heating temperature (°C)	120

### 2.4. Microstructural Characterisation

A scanning electron microscope (SEM, S-3400, Hitachi, Tokyo, Japan) with an energy dispersive spectrometer (EDS) ( $V_{a/c} = 20.0$  kV) was employed to observe the microstructure of the cross-section and the worn surface topographies, as well as for the local elemental analysis. The X-ray diffraction equipment (XRD, Shimadzu 7000, Shimadzu, Kyoto, Japan) using monochromatic Cu K $\alpha$  radiation ( $\lambda = 0.1541$  nm) at 40 kV, 30 mA was used to distinguish the phases composition of the powders and coatings, which had a scanning range of 20°–90° and a scanning speed of 4°/min.

### 2.5. Performance Tests of Coatings

In order to reduce the roughness to less than 0.01  $\mu\text{m}$  and to present mirror conditions, which can minimize the influence of surface roughness on the hardness and tribological properties of the coatings as much as possible, it is necessary to polish the cross section and upper surface of the specimens before the performance tests. After this, the microhardness of the coatings was measured by means of an HVS-1000 Vickers microhardness tester (Jiangdong Kunming, Ningbo, China) with a 0.1-kg (0.98 N) load and 15-s dwell time. The average microhardness value was calculated on the base of ten measurements. In addition, the distance between every two indentations in this experiment is more than three imprints, in order to ensure that the individual indentations do not interfere with each other. The Al<sub>2</sub>O<sub>3</sub> balls (with a diameter of 6 mm) were used as a counterpart to better simulate the actual application environment of the coating blades. The ability of the coatings to resist wear was tested through the ball-on-disk wear test (SFT-2M, Zhongke Kaihua Technology Development Co.,

Lanzhou, China) with a 30-N loading at a sliding speed of 0.4 m/s for 30 min, so the reciprocating wear distance is about 720 m. The experiments were performed in triplicate on the same sample in order to reduce the random error. After the wear test, the three-dimensional morphology of wear scratches was observed through laser scanning confocal microscopy (OLS4100, Olympus, Tokyo, Japan).

### 3. Results and Discussion

#### 3.1. Microstructure and Phase Composition

The XRD analysis results for the NiCr–TiB<sub>2</sub>–ZrB<sub>2</sub> powders are shown in Figure 1. It can be seen that the strongest peaks are attributed to Ni, while the remaining small peaks are referred to TiB<sub>2</sub> and ZrB<sub>2</sub> as well as the newly generated CrB phase. This meant that the powders obtained energy during the ball milling process, which led to the decomposition of the old phases (NiCr, TiB<sub>2</sub>, and ZrB<sub>2</sub>) and the generation of the new phase (CrB). In addition, there were no common oxidation phases [20], such as TiO<sub>2</sub>, Ti<sub>2</sub>O<sub>3</sub>, NiTiO<sub>3</sub>, and ZrO<sub>2</sub> that reduced the performance of the coating in the powders prepared using the high-energy ball milling method, which illustrates that the quality of the powders is relatively good.

The XRD diagrams of the three powders are almost the same, except for the different intensity of the peaks. This may be because the composition of the three powders is consistent, but the proportions of each powder are different, which leads to a difference in the content of the reactants, even under the same ball milling parameters. It can also be seen from Figure 1 that with an increase in the TiB<sub>2</sub> and ZrB<sub>2</sub> content, the corresponding peak intensity gradually increases, but the change in CrB is relatively small. The mechanism of the content of the generated materials needs further study.

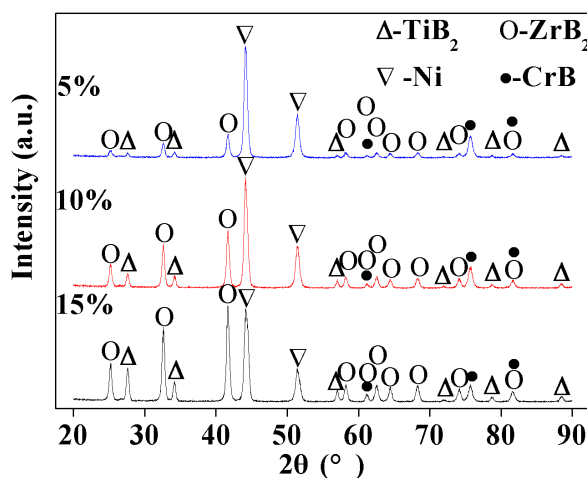


**Figure 1.** X-ray diffraction (XRD) spectra of three kinds of NiCr–TiB<sub>2</sub>–ZrB<sub>2</sub> powders.

The XRD patterns obtained from the top surface of the as-deposited coatings are shown in Figure 2. It was found that the ceramic reinforcement phases of TiB<sub>2</sub> and ZrB<sub>2</sub> still exist in the coatings, although the peak intensities are significantly lower compared with the mixed powders. This is a good indication that the TiB<sub>2</sub> and ZrB<sub>2</sub> phases in the coatings are the un-reacted reactants from the starting powders, not the new generators. It is difficult to decompose the TiB<sub>2</sub> and ZrB<sub>2</sub> particles during the rapid melting and solidification process, so they are used to prepare the ceramic reinforced base coatings in this experiment. In addition, there are also some minor peaks existing in the coatings, such as BNi<sub>2</sub> and Ni<sub>4</sub>B<sub>3</sub>. These minor peaks can be attributed to the liberated particles formed by a small amount of decomposition of the TiB<sub>2</sub> and ZrB<sub>2</sub> particles that chemically react with NiCr.

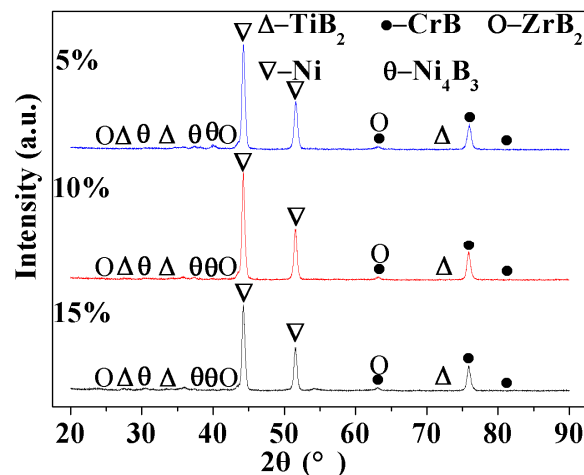


Figure 2. X-ray diffraction (XRD) spectra of three kinds of NiCr-TiB<sub>2</sub>-ZrB<sub>2</sub> coatings.

Figure 3 shows the upper surface morphology of the NiCr-15ZrB<sub>2</sub>-15ZrB<sub>2</sub> composite coatings with the distribution of all of the elements. The process of the mechanical stacking of plasma spraying powders is clearly shown in Figure 3a, and the pores of the coating were small, which proved that the density of the coating was relatively good. In addition, ZrB<sub>2</sub>, TiB<sub>2</sub>, and the compounds of the Ni, B, and Cr existing in the coating can be analyzed from Figure 3a–f and the results of the XRD.

The cross-sectional morphology of the NiCr-TiB<sub>2</sub>-ZrB<sub>2</sub> composite coating using different proportions of source materials in Figure 4, showed that all of the coatings had a dense layered structure [21]. This is due to the fact that individual particles are rapidly heated and accelerated by Ar and H<sub>2</sub> in air plasma spraying. Typically, these particles are partially melted before being deposited in the substrate, because the temperature is already close to the melting point of the materials (3000 °C). After this, they will quickly cool to a lower temperature and flatten to form a thin sheet when they hit the substrate.

As observed from Figure 4a,c,e, the thicknesses of the composite coatings are in the range of 150–200 μm. All of the coatings have a small amount of porosity, especially in the interface between the coating and the substrate. This may be because the temperature difference between the coating and substrate is large, so the deformations of the particles have a significantly condensation contraction in this area, which finally produce pores. Furthermore, pores are also formed when there is not a complete covering between the different layers during the process of the coating deposition [22].

As seen from Figure 4b,d,f, the porosity of the coatings increases with increase of the ceramic phases. This may be due to the spraying process, as the degree of rebound of the ceramic phases is much greater than that of the metallic binder phases. Thus, with an increase in the ceramic phases, the gaps in the coating process increase gradually and the degree of melting of the ceramic phases is considerably less than the metal bonding phase. This reduces the probability that these gaps will be filled in time, resulting in an increased porosity. In addition, although this reduces the porosity of the three types of coatings, increasing the content of the bonding phase can significantly reduce the probability of the ceramic phase rebound, which subsequently reduces the porosity [23,24].

Based on the microstructure of Figure 4 and the energy spectrum data in Table 3, the phase composition of the coating can be simply divided into three categories. Firstly, the areas colored in black (A, F, and I in Figure 4) contain the pure TiB<sub>2</sub> that exists alone in the coatings. They are surrounded by large areas of grey bonding phases (Ni, CrB, BNi<sub>2</sub>, and Ni<sub>4</sub>B<sub>3</sub>), as shown in B, E, and H in Figure 4. There are also striped mixed phases (C, D, and G in Figure 4), which contain bonding phases and ZrB<sub>2</sub>. As the color of the stripe becomes darker, the concentration of ZrB<sub>2</sub> increases gradually. In these coatings, the wear resistance is mainly provided by the TiB<sub>2</sub> and ZrB<sub>2</sub> phases, while the bonding phases mainly increase the toughness and reduce the difference of the coefficients of

expansion between the substrate and the coating. Therefore, a reasonable proportion of ceramic/metal can be conducive to improve the comprehensive performance of the coating.

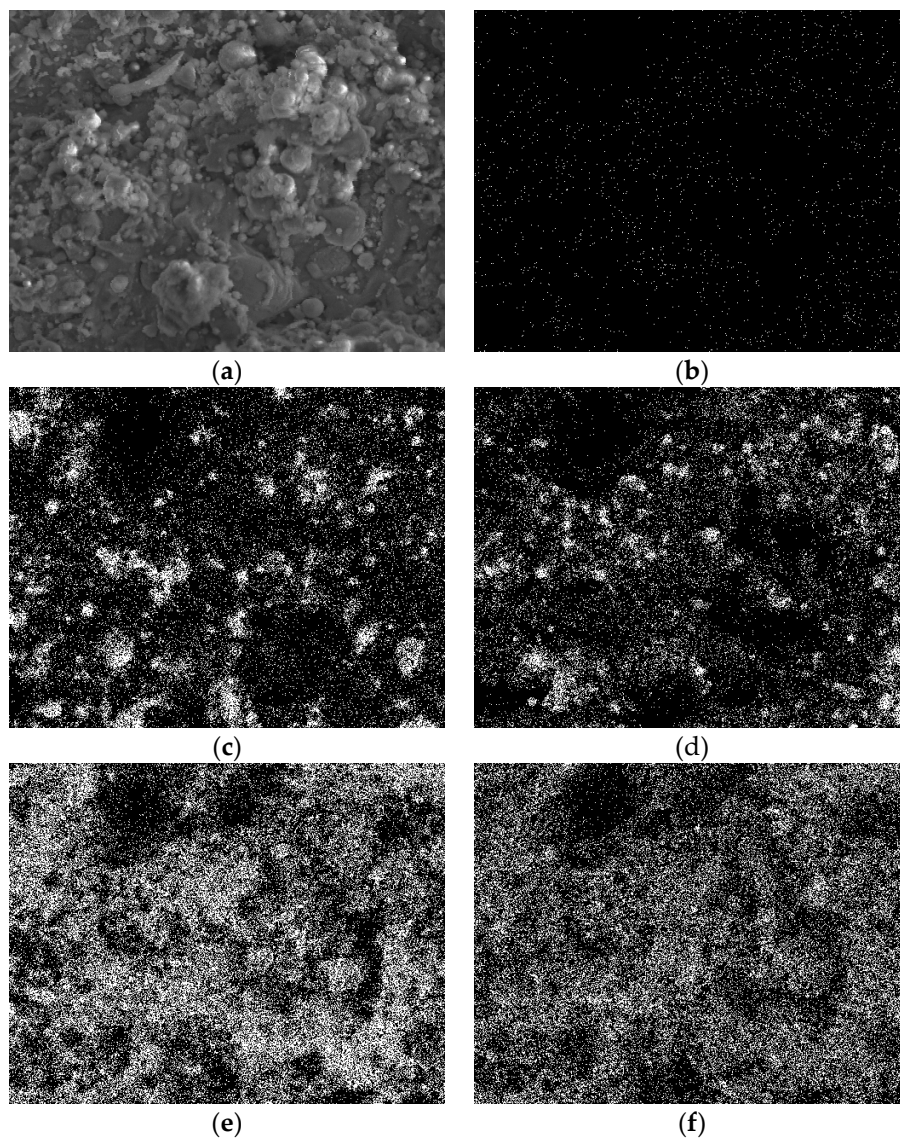


**Figure 3.** Elements distribution on the upper surface of NiCr-TiB<sub>2</sub>-ZrB<sub>2</sub> coating: (a) NiCr-TiB<sub>2</sub>-ZrB<sub>2</sub> coating; (b) B; (c) Ti; (d) Zr; (e) Ni; and (f) Cr.

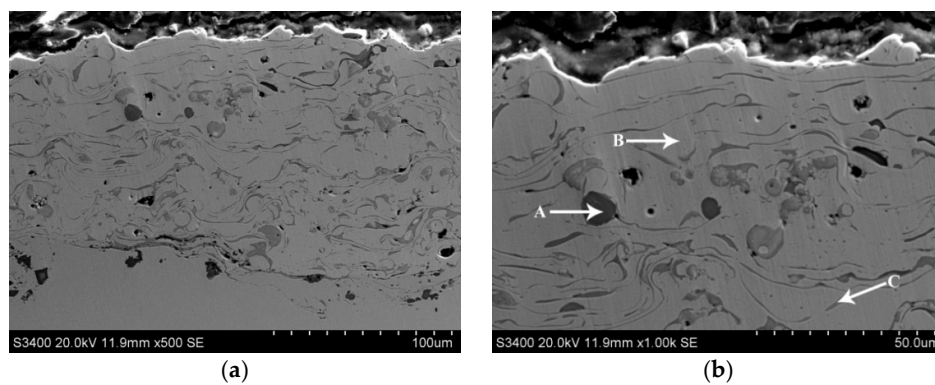


**Figure 4.** Cont.

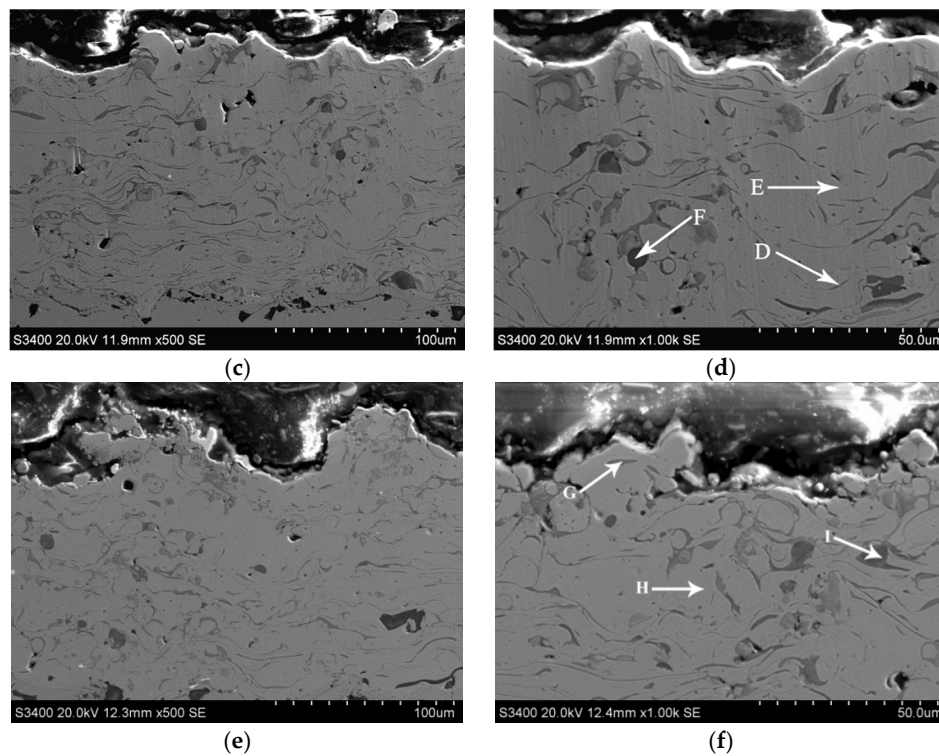


**Figure 4.** Microstructure of the coatings: (a)  $5\text{TiB}_2\text{-}5\text{ZrB}_2\text{-NiCr}$ ; (b) higher magnification image of  $5\text{TiB}_2\text{-}5\text{ZrB}_2\text{-NiCr}$ ; (c)  $10\text{TiB}_2\text{-}10\text{ZrB}_2\text{-NiCr}$ ; (d) higher magnification image of  $10\text{TiB}_2\text{-}10\text{ZrB}_2\text{-NiCr}$ ; (e)  $15\text{TiB}_2\text{-}15\text{ZrB}_2\text{-NiCr}$ ; and (f) higher magnification image of  $15\text{TiB}_2\text{-}15\text{ZrB}_2\text{-NiCr}$ .

**Table 3.** Chemical composition (at.%) in different regions in Figure 4.

Zone	Ni	Cr	Zr	Ti	B
A	–	–	–	34.21	65.79
B	72.43	15.98	0.24	0.62	10.73
C	15.93	19.98	10.07	12.41	41.61
D	29.95	14.95	10.71	7.82	36.57
E	61.13	17.64	0.62	1.25	19.36
F	–	–	–	36.47	63.53
G	20.68	12.06	5.73	13.70	47.83
H	65.43	14.91	0.11	0.83	18.72
I	–	–	–	33.52	66.48

### 3.2. Performance Test of Coatings

It can be seen from Figure 5 that the average hardness obtained on the coating cross-section was 753, 957, and 1102  $\text{HV}_{0.1}$ , respectively. However, the microhardness value of each coating was floating up and down in a range. This is due to several reasons. Firstly, the parts of the ceramic phases do not dissolve in the bonding phases, which prevents uniform hardness. Furthermore, the presence of fine pores will reduce the hardness. In addition, it is attributed to the high hardness of the ceramic phases, as an increase in the proportion of ceramic results in a gradual increase in the hardness of the composite coating. Moreover, the generally accepted opinion in the field of friction and wear is that the ceramic phases in the metal ceramic composite coating are mainly able to provide wear resistance to the coating because of their high hardness. The main role of the metal phase is to maximize the retention of the ceramic phases in the coating and to improve the ductility of the coating and the bonding strength between the substrate materials due to the high toughness and the coefficient of thermal expansion being similar to the substrate. Therefore, a higher content of ceramic phases results

in a greater hardness and better wear resistance when the toughness and bonding strength fulfill the requirements.

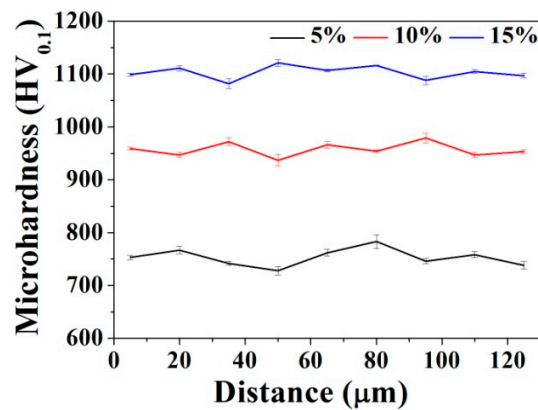


Figure 5. Microhardness value of the coatings.

The Weibull distribution is widely used in reliability engineering as we can easily infer its distribution parameters using probability values. The coating contains two types of phases (hard phase and binder phase) with a large difference in hardness, and the hardness measurement in the experiment is random, so the Weibull distribution can be used in this paper to analyze the continuity of the coating hardness from the view of probability and statistics. The formula can be described as follows [25]:

$$F(H) = 1 - \exp[-(H/\eta)^\beta] \tag{1}$$

where  $H$  is the hardness data,  $\beta$  is the Weibull shape parameter, and  $\eta$  is a normalized tested parameter. The equation can also be transformed into the following:

$$\ln[-\ln(-F(H))] = \beta[\ln(H) - \ln(\eta)] \tag{2}$$

As shown in Figure 6, all of the points can be synthesized into a straight line and the equations ( $y = \beta x + b$ ) and reliability parameter ( $R$ ) are listed separately in each diagram. With the addition of the ceramic phases ( $\text{TiB}_2$  and  $\text{ZrB}_2$ ), the  $\beta$  values of the coatings rose from 67.39 to 134.28, implying that the coating had a minimal variation when the content of the ceramic phases ( $\text{TiB}_2$  and  $\text{ZrB}_2$ ) in the powder reached 30% [26]. However, the range of the  $R$  values was 0 to 1, and an increase in the  $R$  value resulted in an increase in the coating stability. In addition, the  $R$  value of all of the coatings is greater than 0.9 and it can be seen that the overall change of the coatings was small.

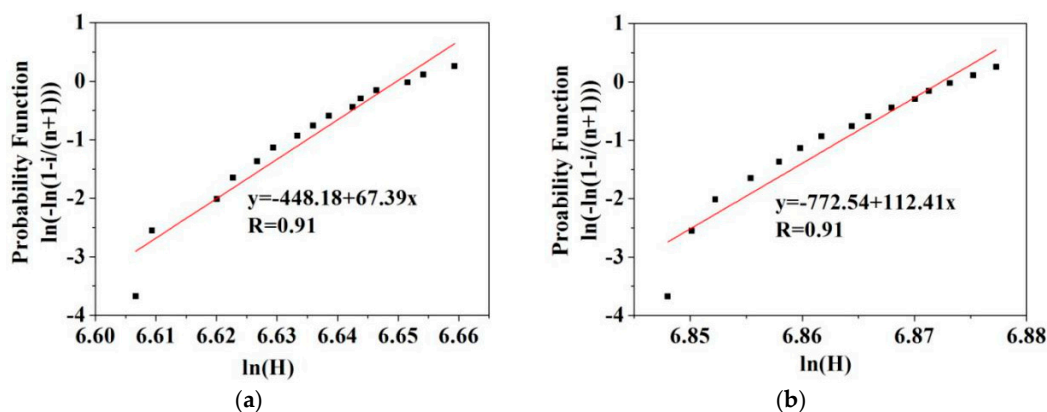
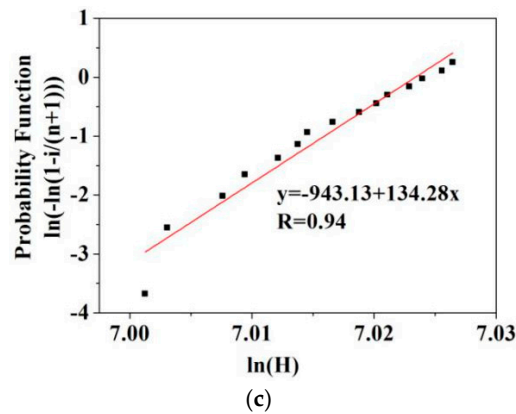


Figure 6. Cont.



**Figure 6.** Linear fit of Weibull distribution of each load: (a) NiCr-5TiB<sub>2</sub>-5ZrB<sub>2</sub>; (b) NiCr-10TiB<sub>2</sub>-10ZrB<sub>2</sub>; and (c) NiCr-15TiB<sub>2</sub>-15ZrB<sub>2</sub>.

It can be seen from Figure 7 that the average friction coefficient curves of the three types of NiCr-TiB<sub>2</sub>-ZrB<sub>2</sub> composite coatings against the Al<sub>2</sub>O<sub>3</sub> ball were approximately 0.57, 0.50, and 0.45 in the steady wear stage, respectively. The friction coefficient is lower, with a large fluctuation found in the running-in stage, which may be attributed to the changes in the surface roughness. In general, the coefficient of friction is mainly related to the test parameters, the properties of materials, surface roughness, and lubrication state between the sample and grinding material (Al<sub>2</sub>O<sub>3</sub>). Considering that the three types of experiments differ only in the material composition, it can be understood that increasing the number of ceramic phases can reduce the friction coefficient of the coatings, which indicates that the ceramic phases are appropriate reinforcements to further enhance the wear resistance of the composite coatings. Moreover, as seen from the curves in Figure 6, the friction coefficients become more stable with an increase in the content of the ceramic phases, especially in the content of the ceramic phases TiB<sub>2</sub> and ZrB<sub>2</sub>, which increased from 20 to 30 wt.%.

Figures 8–10 separately show the average wear depth and mass loss of NiCr-TiB<sub>2</sub>-ZrB<sub>2</sub> composite coatings after the wear test, while the surface topographies corresponding to the mapping in Figure 9 are inserted in the top-left. They show a trend that is similar to the friction coefficient of the NiCr-TiB<sub>2</sub>-ZrB<sub>2</sub> (Figure 6), which gradually decreases with the increased content of the ceramic phases, although the decreasing trend was less marked. In addition, the NiCr-15TiB<sub>2</sub>-15ZrB<sub>2</sub> had a minimal wear loss (0.00784 g) and the shallowest wear depth (19 μm) of about 39.17% and 60.31% of the maximum, respectively, which showed the best anti-wear performance among the three types of coating.

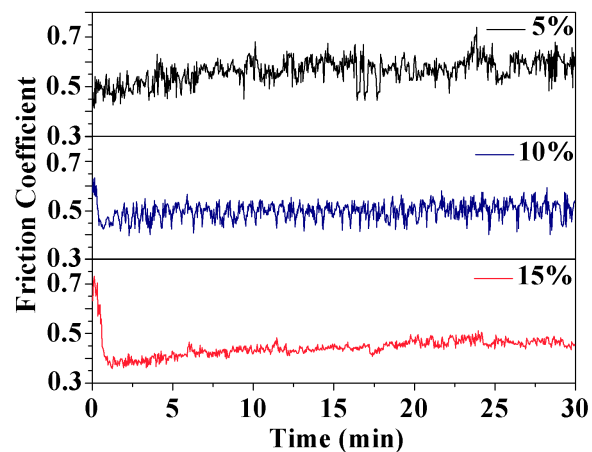


**Figure 7.** Friction coefficient of the NiCr-TiB<sub>2</sub>-ZrB<sub>2</sub> coatings.

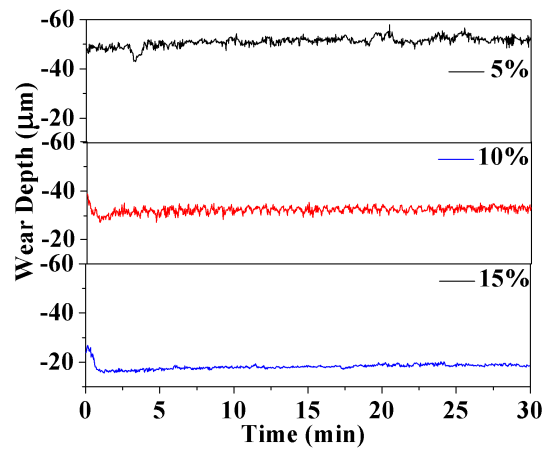


Figure 8. Wear depth of NiCr–TiB<sub>2</sub>–ZrB<sub>2</sub> coatings.

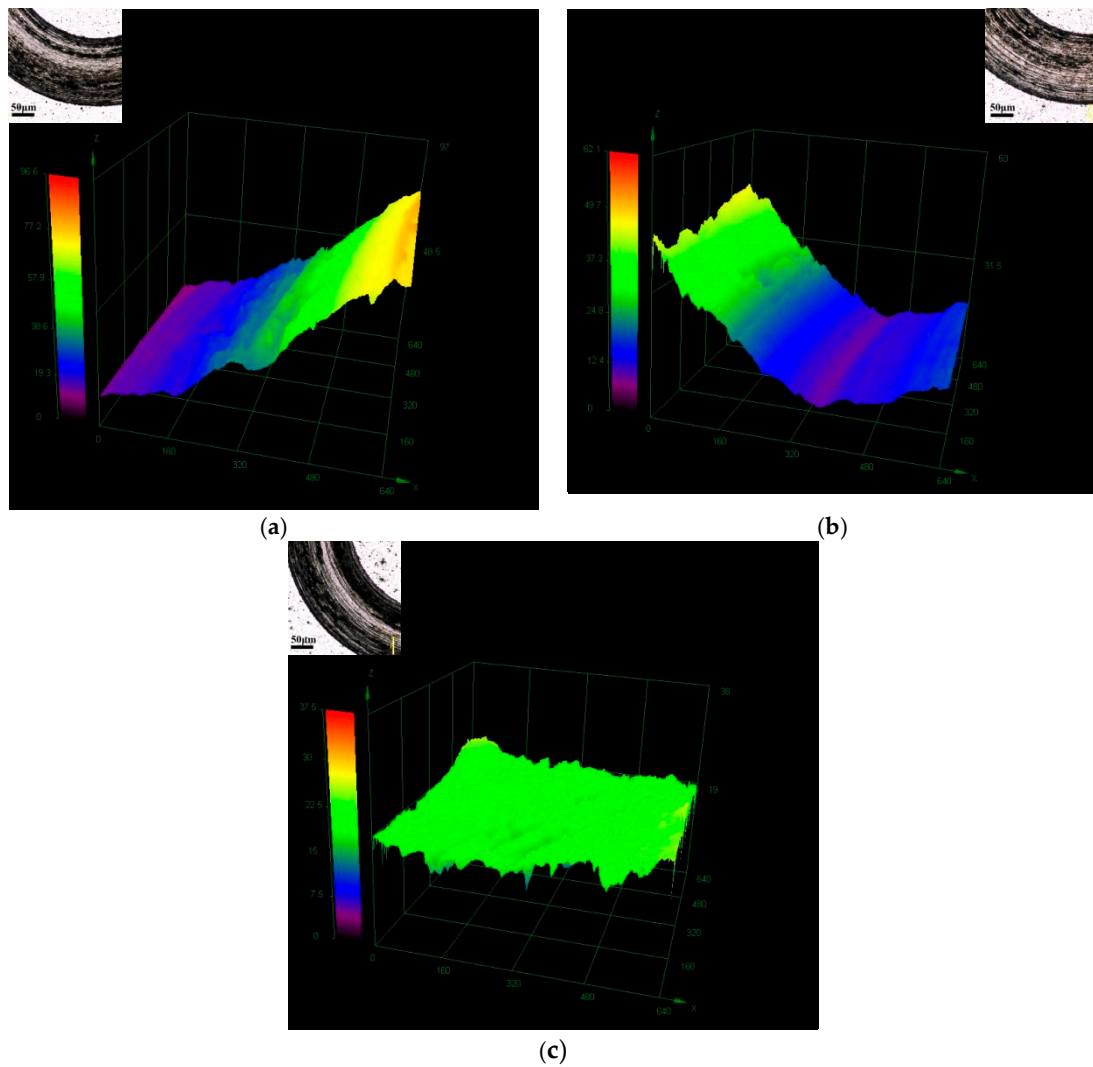


Figure 9. Three-dimensional (3D) non-contact surface mapping of the wear scars of (a) NiCr–5TiB<sub>2</sub>–5ZrB<sub>2</sub>; (b) NiCr–10TiB<sub>2</sub>–10ZrB<sub>2</sub>; and (c) NiCr–15TiB<sub>2</sub>–15ZrB<sub>2</sub>.

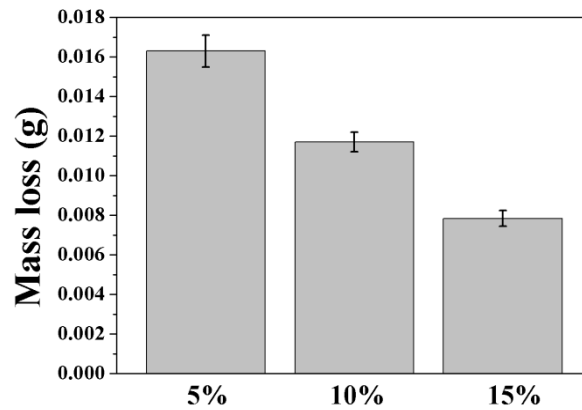


Figure 10. Mass loss of the NiCr–TiB<sub>2</sub>–ZrB<sub>2</sub> coatings.

To better understand the wear behaviour of the NiCr–TiB<sub>2</sub>–ZrB<sub>2</sub> composite coatings, SEM morphologies and EDS analyses (Table 4) of the worn surfaces are shown in Figure 11. As shown in Figure 11a, the worn surface of NiCr–5TiB<sub>2</sub>–ZrB<sub>2</sub> was characterised by superficial and narrow grooves (zones A, D, and H), adhesive craters and a few cracks (zone B) with severe plastic deformation, oxygen element (zones C, E, G, and J) (from Table 4), TiB<sub>2</sub> phases (zones F and I) (from Table 4), and the white light zone. This implies that abrasive wear, adhesive wear, fatigue wear, and oxidation wear occurred.

During the test, the temperature between the coating and the counterbody increased gradually with a prolonged operation time, and thus, the adhesion between them may occur as a result of the direct contact. Through the research of Kliagua [27], this adhesion occurred between a ceramic material and cermet under a high temperature and high pressure. Therefore, the splats on the surface of the coating can adhere to the ball before being dragged out, which caused the emergence of the transfer layer. The peeling of the splats can be attributed to the limited interlamellar bonding, which was very common in the thermal-sprayed coatings [28]. The EDS analysis results showed that the white zones were oxidized with an oxygen content of up to 16.94 at.% (Table 4). The friction process released heat and caused an increase in the temperature on the upper sliding surface, which finally leads to oxidation. In addition, the oxidized phases can be crushed, and fine oxide particles were formed. Under the load applied, these fine oxide particles played the part of ploughs and the furrows along the sliding direction formed. It was reported that the fatigue wear resistance of the materials increased with the surface hardness [29]. Hence, when the hardness of the materials was lower, the probability of fatigue wear increased with the increasing wear time.

Many fragments of wear debris were also accumulated (Figure 11b–d), the morphologies of which were similar to the NiCr–5TiB<sub>2</sub>–ZrB<sub>2</sub> coating, except for the cracks. However, the degree of adhesive wear gradually decreased, which may be because the hardness of the coatings rose significantly. In addition, the NiCr–15TiB<sub>2</sub>–15ZrB<sub>2</sub> composite coating had the best tribological properties.

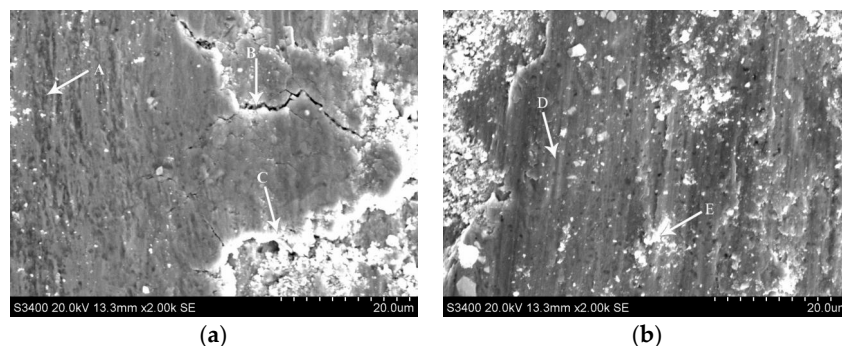
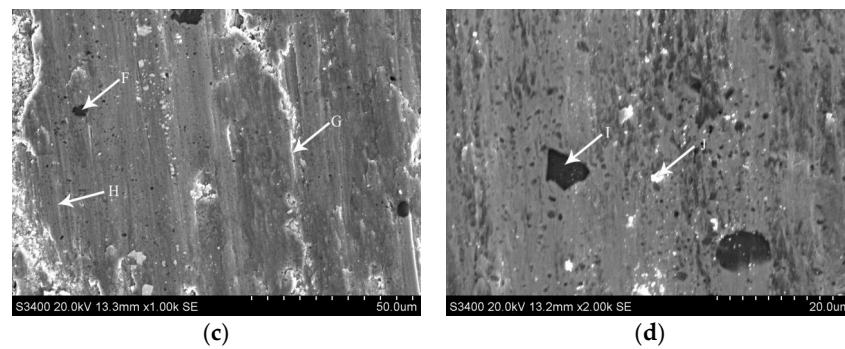


Figure 11. Cont.



**Figure 11.** Worn morphologies of surface: (a) NiCr-5TiB<sub>2</sub>-5ZrB<sub>2</sub>; (b) NiCr-10TiB<sub>2</sub>-10ZrB<sub>2</sub>; (c) NiCr-15TiB<sub>2</sub>-15ZrB<sub>2</sub>; and (d) higher magnification image NiCr-15TiB<sub>2</sub>-15ZrB<sub>2</sub>.

**Table 4.** Chemical composition (at.%) in different regions in Figure 11.

Zone	Ni	Cr	Ti	Zr	B	O
C	47.86	12.69	2.86	1.29	18.36	16.94
E	42.89	10.43	4.07	3.11	25.87	13.63
F	–	–	33.54	–	66.46	–
I	–	–	34.73	–	65.27	–
J	35.97	8.54	5.66	3.29	34.72	11.82

#### 4. Conclusions

The NiCr-TiB<sub>2</sub>-ZrB<sub>2</sub> composite coatings were successfully fabricated on the SUS304 surface using high-energy ball milling and air plasma spraying technology. The microstructure and mechanical properties of the NiCr-TiB<sub>2</sub>-ZrB<sub>2</sub> coatings with various TiB<sub>2</sub> and ZrB<sub>2</sub> contents were investigated. The following results can be highlighted:

- With an increase in the proportion of ceramics, the microhardness of the composite coating gradually increased. The average hardness obtained on the coating cross-section was 753, 957, and 1102 HV<sub>0.1</sub> for NiCr (5 wt.%)–TiB<sub>2</sub> (5 wt.%)–ZrB<sub>2</sub>, NiCr (10 wt.%)–TiB<sub>2</sub> (10 wt.%)–ZrB<sub>2</sub>, and NiCr (15 wt.%)–TiB<sub>2</sub> (15 wt.%)–ZrB<sub>2</sub> coatings.
- From the analyses of the Weibull distributions, the *R* value of all of the coatings was greater than 0.9 and there was little overall change of the coatings. With the addition of the ceramic phases (TiB<sub>2</sub> and ZrB<sub>2</sub>), the β-values of the coatings rose from 67.39 to 134.28, implying that the coating had a minimal variation when the content of the ceramic phases (TiB<sub>2</sub> and ZrB<sub>2</sub>) increased.
- The wear mechanism of the coatings was mixed, involving abrasive wear, adhesive wear, oxidation wear, and fatigue wear. The ceramic phases in the coatings gave outstanding resistance to wear and oxidation. The NiCr-15TiB<sub>2</sub>-15ZrB<sub>2</sub> composite coating had the best tribological properties.

**Author Contributions:** Investigation, N.Z.; Conceptualization and Supervision, N.N.Z.; SEM (scanning electron microscope) Analysis, S.G.; XRD (X-ray diffraction) Analysis, S.L.; Data Reduction, G.Z.; Writing–Original Draft, N.Z.; Writing–Review & Editing, Y.Z.

**Funding:** This research was funded by the Natural Science Foundation of Liaoning Province (201602553) and Chinese National Natural Science Foundation (51301112).

**Acknowledgments:** Thanks to Yingdong Qu for giving help on the wearing surface observation.

**Conflicts of Interest:** The authors declare no conflict of interest.

#### References

1. Alam, P.; Toivakka, M. Deflection and plasticity of soft-tip bevelled blades in paper coating operations. *Mater. Design* **2009**, *30*, 871–877. [[CrossRef](#)]

2. Hua, Y.; Xu, L.; Hua, W. Development of tungsten carbide blade. *Chin. Pulp. Pap.* **2013**, *32*, 49–52. [[CrossRef](#)]
3. Wang, H.; Li, H.; Zhu, H.; Cheng, F.; Wang, D.; Li, Z. A comparative study of plasma sprayed TiB<sub>2</sub>-NiCr and Cr<sub>3</sub>C<sub>2</sub>-NiCr composite coatings. *Mater. Lett.* **2015**, *153*, 110–113. [[CrossRef](#)]
4. Zhang, C.; Luo, G.; Zhang, J.; Dai, Y.; Shen, Q.; Zhang, L. Synthesis and thermal conductivity improvement of W-Cu composites modified with WC interfacial layer. *Mater. Design* **2017**, *127*, 233–242. [[CrossRef](#)]
5. Zhang, Y.; Ma, J. Tungsten carbide ceramics. In *Practical Handbook of Ceramic Materials*, 1st ed.; Chemical Industry Press: Beijing, China, 2006; pp. 390–399. ISBN 7-5025-8469-2. (In Chinese)
6. Vashishtha, N.; Khatirkar, R.K.; Sapate, S.G. Tribological behaviour of HVOF sprayed WC-12Co, WC-10Co-4Cr and Cr<sub>3</sub>C<sub>2</sub>-25NiCr coatings. *Tribol. Int.* **2017**, *105*, 55–68. [[CrossRef](#)]
7. Zhu, H.B.; Li, H.; Li, Z.X. Plasma sprayed TiB<sub>2</sub>-Ni cermet coatings: Effect of feedstock characteristics on the microstructure and tribological performance. *Surf. Coat. Technol.* **2013**, *235*, 620–627. [[CrossRef](#)]
8. Zhang, Y.; Yu, F.; Hao, S.; Dong, F.; Xu, Y.; Geng, W.; Zhang, N.; Gey, N.; Grosdidier, T.; Dong, C. Evolution of nanostructure and metastable phases at the surface of a HCPEB-treated WC-6% Co hard alloy with increasing irradiation pulse numbers. *Coatings* **2017**, *7*, 178. [[CrossRef](#)]
9. Zhang, M.; Qu, K.; Luo, S.; Liu, S. Effect of Cr on the microstructure and properties of TiC-TiB<sub>2</sub> particles reinforced Fe-based composite coatings. *Surf. Coat. Technol.* **2017**, *316*, 131–137. [[CrossRef](#)]
10. Yan, H.; Zhang, P.; Yu, Z.; Lu, Q.; Yang, S.; Li, C. Microstructure and tribological properties of laser-clad Ni-Cr/TiB<sub>2</sub> composite coatings on copper with the addition of CaF<sub>2</sub>. *Surf. Coat. Technol.* **2012**, *206*, 4046–4053. [[CrossRef](#)]
11. Lotfi, B.; Shipway, P.H.; McCartney, D.G.; Edris, H. Abrasive wear behaviour of Ni(Cr)-TiB<sub>2</sub> coatings deposited by HVOF spraying of SHS-derived cermet powders. *Wear* **2003**, *254*, 340–349. [[CrossRef](#)]
12. Jones, M.; Horlock, A.J.; Shipway, P.H.; McCartney, D.G.; Wood, J.V. A comparison of the abrasive wear behavior of HVOF sprayed titanium carbide-and titanium boride-based cermet coatings. *Wear* **2001**, *251*, 1009–1016. [[CrossRef](#)]
13. Xu, J.; Zou, B.; Zhao, S.; Hui, Y.; Huang, W.; Zhou, X.; Wang, Y.; Cai, X.; Cao, X. Fabrication and properties of ZrC-ZrB<sub>2</sub>/Ni cermet coatings on a magnesium alloy by atmospheric plasma spraying of SHS powders. *Ceram. Int.* **2014**, *40*, 1537–1554. [[CrossRef](#)]
14. Umanskyi, O.; Poliarus, O.; Ukrainets, M.; Antonov, M.; Hussainova, I. High temperature sliding wear of NiAl-based coatings reinforced by borides. *Mater. Sci.* **2016**, *22*, 49–53. [[CrossRef](#)]
15. Farhadinia, F.; Sedghi, A. Wear behaviour of Al/(Al<sub>2</sub>O<sub>3</sub> + ZrB<sub>2</sub> + TiB<sub>2</sub>) hybrid composites fabricated by hot pressing. *Int. J. Mater. Res.* **2015**, *106*, 160–165. [[CrossRef](#)]
16. Chakraborty, S.; Debnath, D.; Mallick, A.R.; Das, P.K. Mechanical and thermal properties of hot pressed ZrB<sub>2</sub> system with TiB<sub>2</sub>. *Int. J. Refract. Met. Hard Mater.* **2014**, *46*, 35–42. [[CrossRef](#)]
17. Li, B. Effect of ZrB<sub>2</sub> and SiC addition on TiB<sub>2</sub>-based ceramic composites prepared by spark plasma sintering. *Int. J. Refract. Met. Hard Mater.* **2014**, *46*, 84–89. [[CrossRef](#)]
18. Luo, P.; Xiong, C.; Wang, C.; Qin, F.; Xiao, Y.; Li, Z.; Liu, K.; Guan, X.; Dong, S. Comparative failure analysis of electrodes coated with TiB<sub>2</sub>-ZrB<sub>2</sub> and TiB<sub>2</sub>-ZrB<sub>2</sub>/Ni layers. *Surf. Coat. Technol.* **2017**, *317*, 83–94. [[CrossRef](#)]
19. Zhang, L.; Wang, C.; Qian, S.; Yu, Q.; Dong, C. Microstructure and wear resistance of laser-clad (Co,Ni)<sub>61.2</sub>B<sub>26.2</sub>Si<sub>7.8</sub>Ta<sub>4.8</sub> coatings. *Metals* **2017**, *7*, 419. [[CrossRef](#)]
20. Wu, Y.; Zeng, D.; Liu, Z.; Qiu, W.; Zhong, X.; Yu, H.; Li, S. Microstructure and sliding wear behavior of nanostructured Ni<sub>60</sub>-TiB<sub>2</sub> composite coating sprayed by HVOF technique. *Surf. Coat. Technol.* **2011**, *206*, 1102–1108. [[CrossRef](#)]
21. Zhang, N.; Lin, D.; He, B.; Zhang, G.; Li, D. Effect of oxyacetylene flame remelting on wear behaviour of supersonic air-plasma sprayed NiCrBSi/h-BN composite coatings. *Surf. Rev. Lett.* **2017**, *24*, 83–90. [[CrossRef](#)]
22. Pawlowski, L. Coating growth. In *The Science and Engineering of Thermal Spray Coatings*, 1st ed.; Li, H., He, D., Eds.; China Machine Press: Beijing, China, 2011; pp. 135–136. ISBN 978-7-111-32163-7. (In Chinese)
23. Zhang, N.; Zhang, N.; Wei, X.; Zhang, Y.; Li, D. Microstructure and tribological performance of TiB<sub>2</sub>-NiCr composite coating deposited by APS. *Coatings* **2017**, *7*, 238. [[CrossRef](#)]
24. Zhu, H.; Li, H.; Yang, H.; Li, Z. Microstructure and sliding wear performance of plasma-sprayed TiB<sub>2</sub>-Ni coating deposited from agglomerated and sintered powder. *J. Therm. Spray. Technol.* **2013**, *22*, 1310–1319. [[CrossRef](#)]

25. An, Y.; Li, S.; Hou, G.; Zhao, X.; Zhou, H.; Chen, J. Mechanical and tribological properties of nano/micro composite alumina coatings fabricated by atmospheric plasma spraying. *Ceram. Int.* **2017**, *43*, 5319–5328. [[CrossRef](#)]
26. Zhang, F.; He, J.; Chen, K.; Qin, Y.; Li, C.; Yin, F. Microstructure evolution and mechanical properties of TiCN-Cr nano/micro composite coatings prepared by reactive plasma spraying. *Appl. Surf. Sci.* **2017**, *427*, 905–914. [[CrossRef](#)]
27. Kliagua, A.M.; Travessa, D.; Ferrante, M. Al<sub>2</sub>O<sub>3</sub>/Ti interlayer/AISI 304 diffusion bonded joint: Microstructural characterization of the two interfaces. *Mater. Charact.* **2001**, *46*, 65–74. [[CrossRef](#)]
28. Tian, L.; Feng, Z.; Xiong, W. Microstructure, microhardness, and wear resistance of AlCoCrFeNiTi/Ni60 coating by plasma spraying. *Coatings* **2018**, *8*, 112. [[CrossRef](#)]
29. Lu, Z.; Zhou, Y.; Rao, Q.; Jin, Z. An investigation of the abrasive wear behavior of ductile cast iron. *J. Mater. Process. Technol.* **2001**, *116*, 176–181. [[CrossRef](#)]



© 2018 by the authors. Licensee MDPI, Basel, Switzerland. This article is an open access article distributed under the terms and conditions of the Creative Commons Attribution (CC BY) license (<http://creativecommons.org/licenses/by/4.0/>).